OPEN

NPG Asia Materials (2013) 5, e70; doi:10.1038/am.2013.56

www.nature.com/am

ORIGINAL ARTICLE

β-MnO_2 nanorods with exposed tunnel structures as high-performance cathode materials for sodium-ion batteries

Dawei Su[1], Hyo-Jun Ahn[2] and Guoxiu Wang[1]

Sodium-ion batteries are being considered as a promising system for stationary energy storage and conversion, owing to the natural abundance of sodium. It is important to develop new cathode and anode materials with high capacities for sodium-ion batteries. Herein, we report the synthesis of β-MnO_2 nanorods with exposed tunnel structures by a hydrothermal method. The as-prepared β-MnO_2 nanorods have exposed {111} crystal planes with a high density of (1 × 1) tunnels, which leads to facile sodium ion (Na-ion) insertion and extraction. When applied as cathode materials in sodium-ion batteries, β-MnO_2 nanorods exhibited good electrochemical performance with a high initial Na-ion storage capacity of 350 mAh g^{-1}. β-MnO_2 nanorods also demonstrated a satisfactory high-rate capability as cathode materials for sodium-ion batteries.
NPG Asia Materials (2013) **5,** e70; doi:10.1038/am.2013.56; published online 15 November 2013

Keywords: β-MnO_2; nanorods; cathode material; tunnel structure; sodium-ion batteries

INTRODUCTION

Sodium-ion (Na-ion) batteries have recently been considered as an alternative battery system for large-scale energy storage and conversion due to the availability of low-cost and widespread terrestrial reserves of sodium mineral salts.[1] Na-ion batteries share many similarities with lithium-ion batteries (Li-ion batteries), such as an intercalating cathode and anode, a nonaqueous electrolyte and an ion shuttle mechanism. Computational studies on the voltage, stability and diffusion barrier of Na-ion and Li-ion materials indicate that Na-ion systems are competitive with Li-ion systems.[2] However, the large ionic size of sodium (1.02 Å versus lithium (0.76 Å)) limits the choice of electrode materials for Na-ion batteries. Many cathode materials have been investigated for Na-ion batteries, including phosphate polyanion materials ($NaFePO_4$),[3,4] $Na_4Mn_9O_{18}$,[5–7] fluoride-based cathode materials—$NaMF_3$ (M = Fe, Mn, V and Ni),[8,9] fluorophosphates,[10,11] fluorosulfates,[12–14] and layered transition metal oxides, such as P2-Na_xCoO_2,[15,16] P2-$Na_{2/3}(Fe_{1/2}Mn_{1/2})O_2$,[17] $Na_{2/3}(Ni_{1/3}Fe_{1/3}Mn_{2/3})O_2$,[18] $NaCrO_2$,[19,20] Na_xMnO_2,[21,22] and Na_xVO_2.[23] However, none of the above cathode materials showed satisfactory electrochemical performance in terms of specific capacity, cyclability and high-rate capability. Therefore, the discovery of appropriate electrode materials is crucial for the development of high-performance Na-ion batteries.

Manganese dioxide has large open tunnels, which can provide interstitial spaces for Na-ion storage and transport. Herein, we report the synthesis of single-crystalline β-MnO_2 nanorods with dominantly exposed {111} crystal planes. The {111} crystal plane consists of high-density (1 × 1) tunnels that can facilitate fast Na-ion insertion and extraction during the charge and discharge process. The as-prepared β-MnO_2 nanorods exhibited a high Na-ion storage capacity, a good high-rate capability and a satisfactory cyclability. Furthermore, we also explored the effects of Na-ion intercalation and extraction on cycling using *ex situ* X-ray diffraction (XRD) and transmission electron microscopy (TEM) measurements.

MATERIALS AND METHODS

Synthesis of β-MnO_2 nanorods

β-MnO_2 nanorods were synthesized by a hydrothermal method. In a typical process, 1 mmol $(NH_4)_2S_2O_8$ (Sigma-Aldrich, Castle Hill, NSW, Australia, ⩾99%) and 1 mmol $MnSO_4 \cdot H_2O$ (Sigma-Aldrich, ⩾99%) were dissolved in 20 ml of deionized water. A soft template consisting of 0.2 g of cationic surfactant cetyltrimethylammonium bromide (CTAB) (Sigma-Aldrich, ⩾98%) was added. After stirring for at least 30 min, the precursor solution was treated at 90 °C in a teflon-lined autoclave (25 ml in capacity) for 36 h. The precipitate was cooled down to room temperature naturally, collected and washed with distilled water and ethanol several times. After drying at 60 °C in a vacuum oven overnight, the final products were obtained.

Structural and physical characterization

The crystal structure and phase of the as-prepared materials were characterized by XRD, Siemens D5000 (Bruker Axs. Inc., Madison,

[1]Centre for Clean Energy Technology, Faculty of Science, School of Chemistry and Forensic Science, University of Technology, Sydney, New South Wales, Australia and [2]School of Materials Science and Engineering, Gyeongsang National University, 900 Gazwa-dong, Jinju, Korea
Correspondence: Professor G Wang, Centre for Clean Energy Technology, Faculty of Science, School of Chemistry and Forensic Science, University of Technology, Sydney, New South Wales 2007, Australia
E-mail: Guoxiu.Wang@uts.edu.au
Received 30 April 2013; revised 24 August 2013; accepted 28 August 2013

WI, USA) using Cu K_α radiation at a very slow scanning step of $0.0025^\circ\,s^{-1}$ (8.9 h from 10° to 90°). Rietveld refinement was implemented using the GSAS software suite. The morphology was analyzed by a field emission scanning electron microscope (FESEM, Zeiss Supra 55VP, Carl Zeiss Group, Oberkochen, Germany). The structure details were further characterized by TEM and high-resolution transmission electron microscopy (HRTEM, JEOL JEM-2011). Selected area electron diffraction (SAED) patterns were recorded by a Gatan CCD camera in a digital format. Fourier transform infrared spectroscopy (FT-IR) spectra of the samples were recorded on a Nicolet 6700 Spectrometer (Thermo Fisher Scientific Inc., Waltham, MA, USA) by using potassium bromide (KBr) as the dispersant. The surface area information was collected by N_2 adsorption isotherm using a Micromeritics 3Flex analyzer (Micromeritics Instrument Corporation, Norcross, GA, USA) at 77 K. Brunauer–Emmett–Teller (BET) surface areas were calculated using experimental points at a relative pressure of $P/P_0 = 0.05$–0.25. The pore size distribution was calculated by the Barret–Joyner–Halenda (BJH) method.

Electrochemical testing

The electrodes were prepared by dispersing the as-prepared β-MnO_2 nanorods (70 wt%), acetylene carbon black (20 wt%) and poly(vinylidene fluoride) binder (PVDF, 10 wt%) in *N*-methyl-2-pyrrolidone (NMP) to form a slurry. The resultant slurry was pasted onto an aluminum foil using a doctor blade and dried in a vacuum oven for 12 h, followed by pressing at $200\,kg\,cm^{-2}$. The loading of each electrode is 1.2 mg. The electrochemical measurements were carried out using the two-electrode coin cells (CR2032-type) with Na metal as the reference and counter electrode, and glass microfiber (Whatman) as the separator. The CR2032-type coin cells were assembled in an argon-filled glove box (UniLab, Mbraun, Germany). The electrolyte solution was 1 M $NaClO_4$ dissolved in a mixture of ethylene carbonate (EC) and propylene carbonate (PC) with a volume ratio of 1:1. Cyclic voltammetry (CV) was carried out on a CHI 660C electrochemistry workstation with a scan rate of $0.1\,mV\,s^{-1}$ from 1–4.3 V. The charge-discharge measurements were performed at an ambient temperature, and at different current densities in the voltage range from 1 to 4.3 V. To investigate the sodium driven structural and morphological changes of the as-prepared β-MnO_2 nanorods during the sodium insertion and extraction processes, Swagelok-type cells were assembled. The cells were discharged or charged to the required voltages and then opened in the glove box. The active materials were removed from the electrodes and washed with PC before being used for *ex situ* XRD and TEM analyses. The samples were covered and sealed with parafilm in the glove box to avoid exposure to air. Next, the samples were transferred to the XRD instrument for measurement of the XRD patterns.

RESULTS

Structural characterization of β-MnO_2 nanorods

The crystal phase of the as-prepared β-MnO_2 nanorods was identified by XRD. As shown in Figure 1a, all the diffraction peaks can be indexed to the tetragonal phase with the space group of P42/mnm (JCPDS no. 24-0735). The lattice parameters were refined to be $a = b = 4.388$ Å, $c = 2.873$ Å. No impurity phases were observed. The refined crystal structure projected along the [001] direction is shown in Figure 1b, from which the (1×1) tunnels are presented with a tunnel density of $0.104\,Å^{-2}$ (two tunnels per formula unit). We confirmed that the CTAB was completely removed from β-MnO_2 by the measurement

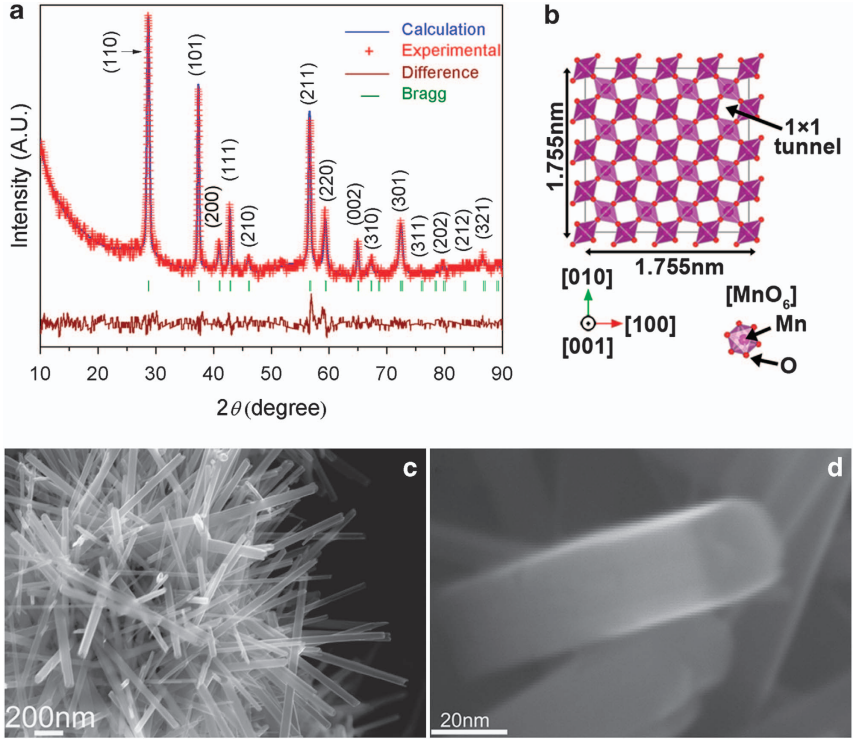

Figure 1 (**a**) Rietveld refinement pattern from the X-ray diffraction data for the β-MnO_2 nanorods; the observed and calculated intensity are represented by red pulses and a blue solid line, respectively. The bottom line shows the fitting residual difference. The Bragg positions are represented as light green ticks ($\chi^2 = 2.2$, $R_{wp} = 6.34\%$, $R_p = 5.08\%$). (**b**) Refined β-MnO_2 crystal structure seen from the [001] orientation. (**c**) Low-magnification field emission scanning electron microscope (FESEM) image of β-MnO_2 nanorods. (**d**) High-magnification FESEM image of β-MnO_2 nanorods, which have a square cross section.

of FTIR spectra of CTAB and β-MnO_2 nanorods (Supplementary Figure S1). The as-prepared β-MnO_2 nanorods have a specific surface area of 14.99 m^2 g^{-1} (as shown in Supplementary Figure S2).

The morphology of β-MnO_2 nanorods were investigated by field emission scanning electron microscope. As shown in Figure 1c, the product consists of 100% one-dimensional (1D) nanorods. The lengths of the β-MnO_2 nanorods extend to a few micrometers. Figure 1d shows a high-magnification view of the cross section of a β-MnO_2 nanorod, which has a square shape with a side length of approximate 20 nm.

The detailed crystal structures of β-MnO_2 nanorods were further analyzed by TEM, SAED and HRTEM analyses (Figure 2). Figure 2a shows a typical low-magnification TEM image of the freestanding β-MnO_2 nanorods, from which it is evident that the individual β-MnO_2 nanorods are well separated. The growth directions of β-MnO_2 nanorods were determined by HRTEM and SAED. As shown in Figure 2b1, the individual β-MnO_2 nanorods grow along the $[\bar{1}\bar{1}2]$ direction, as deduced from the SAED patterns (Figure 2b2). The spot SAED patterns verify the single-crystalline feature of the as-prepared β-MnO_2 nanorods. The rhombic SAED spot patterns can be well indexed along the [111] zone axis of tetragonal β-MnO_2, which indicates that the facet vertical to the electron beam is the (111) crystal plane, and that the two side facets are exposed with $(1\bar{1}0)$ and $(\bar{1}10)$ crystal planes. If this β-MnO_2 nanorod is tilted 34° around the $[\bar{1}\bar{1}2]$ axis (Figure 2c), the contrast of different facets can be observed. Its corresponding SAED spot patterns (Figure 2c2) can be indexed along the [201] zone axis of the tetragonal β-MnO_2. The SAED pattern reflects the combination of the (111) crystal plane and the (110) crystal plane. This further confirms that the enclosed facets of the β-MnO_2 nanorods are {111} and {110} crystal planes, as demonstrated by the geometrical model shown in Figure 2e. From the lattice-resolved HRTEM image (Figure 2d), we can directly observe the regular lattice arrangement of the exposed (111) crystal plane. The crystal structure of the tetragonal β-MnO_2 nanorods is simulated along the [111] direction (the middle inset in Figure 2d). The corresponding Fast-Fourier-Transform (FFT) pattern is shown as the inset in Figure 2d (left-bottom). Figure 2d also shows the $(\bar{1}01)$ and $(\bar{1}10)$ crystal planes with lattice spacings of 0.24 and 0.31 nm and a 67° interfacial angle. As illustrated in Figure 2e, the as-prepared β-MnO_2 nanorods are enclosed with {111} and {110} facets. More TEM images and crystal structural information are shown in Supplementary Figure S3.

Electrochemical properties of β-MnO_2 nanorods for Na-ion storage in Na-ion batteries

β-MnO_2 nanorods were used as cathodes for Na-ion storage in Na-ion batteries. Figure 3a shows the galvanostatic charge–discharge profiles of the β-MnO_2 nanorod electrode in the 1st, 2nd and 100th cycles at a low current density of 20 mA g^{-1}. The galvanostatic charge-discharge profiles are similar to the β-MnO_2 as cathode materials in Li-ion batteries.[24] β-MnO_2 nanorods delivered a high initial discharge capacity of 350 mAh g^{-1}. Although the discharge capacity decreased gradually upon cycling, it still maintained a high value after 100 cycles. The electrochemical reactions during the charge and discharge process were further studied by cyclic voltammetry (as shown in Supplementary Figure S4), from which a pair of redox peaks at 2.4 V and 2.5 V, respectively, were observed.

The cycling performance of the β-MnO_2 nanorods is shown in Figure 3b. The discharge capacity decreases during the initial 20 cycles and then remains stable. A discharge capacity of 192 mAh g^{-1} was achieved after 100 cycles. Figure 4a shows the cycling performance of a β-MnO_2 nanorod electrode charged/discharged at different current densities. The β-MnO_2 nanorod electrode exhibited initial discharge capacities of 280 and 264 mAh g^{-1} at current densities of 50 and 100 mA g^{-1}, respectively. We also examined the high-rate performance of β-MnO_2 nanorods as cathodes in Na-ion batteries. The electrode still delivered a capacity of 118 mAh g^{-1} even when the

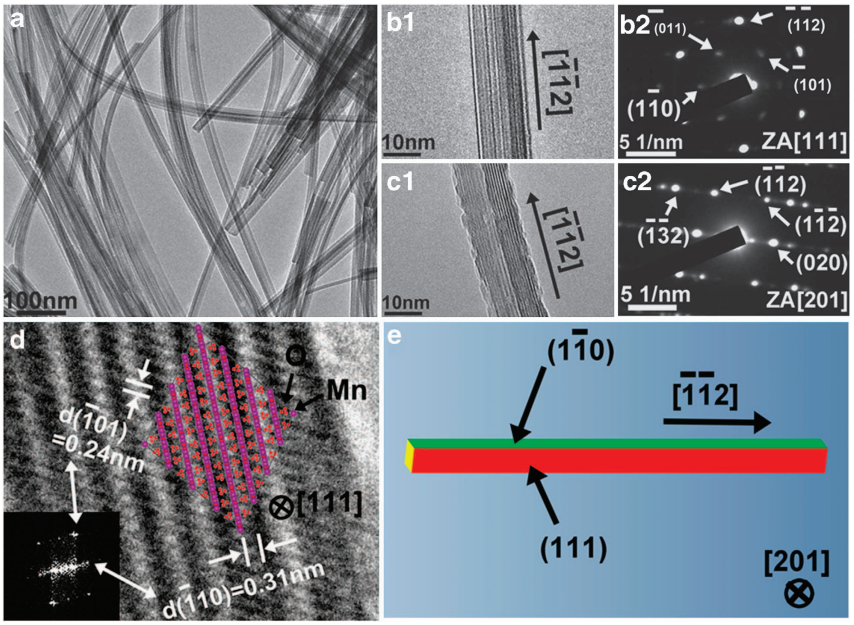

Figure 2 (**a**) Low-magnification TEM images of typical freestanding β-MnO_2 nanorods. (**b1**) High-magnification TEM image of an individual β-MnO_2 nanorod. (**c1**) is the same area imaged in the high-magnification TEM image from **b1** but with a tilt of 34° around the $[\bar{1}\bar{1}2]$ axis. (**b2**) and (**c2**) are the selected area electron diffraction spot patterns (SAED) of (**b1**) and (**c1**), respectively. (**d**) Lattice resolution HRTEM image of β-MnO_2 nanorods. The left bottom inset of **d** is its corresponding fast-Fourier-transform (FFT) patterns, and the middle inset of **d** is the simulated [111] projection of the tetragonal β-MnO_2 crystal structure with several formula units presenting the regular arrangement of atoms (Mn and O marked in purple and red, respectively). (**e**) Geometrical model of β-MnO_2 nanorods, in which different colors represent different crystal planes.

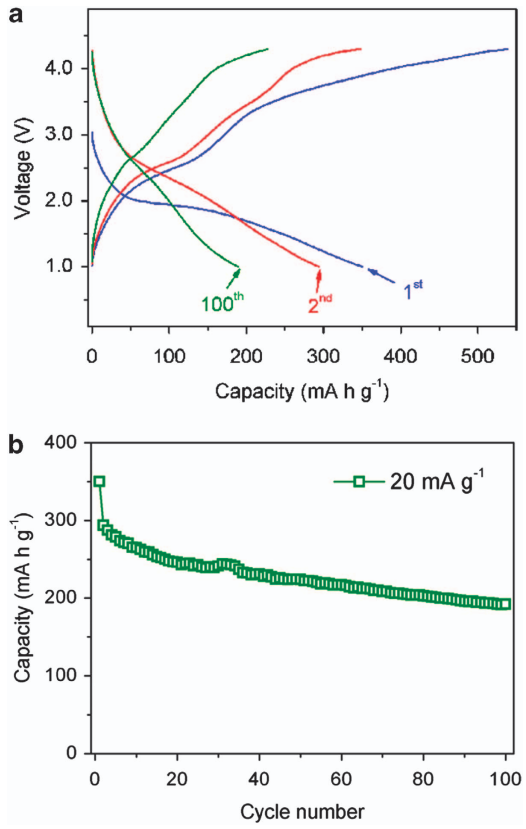

Figure 3 (**a**) The 1st, 2nd and 100th cycle discharge and charge profiles of β-MnO_2 nanorods at a 20 mA g^{-1} current density. (**b**) Cycling performance of β-MnO_2 nanorods at a 20 mA g^{-1} current density.

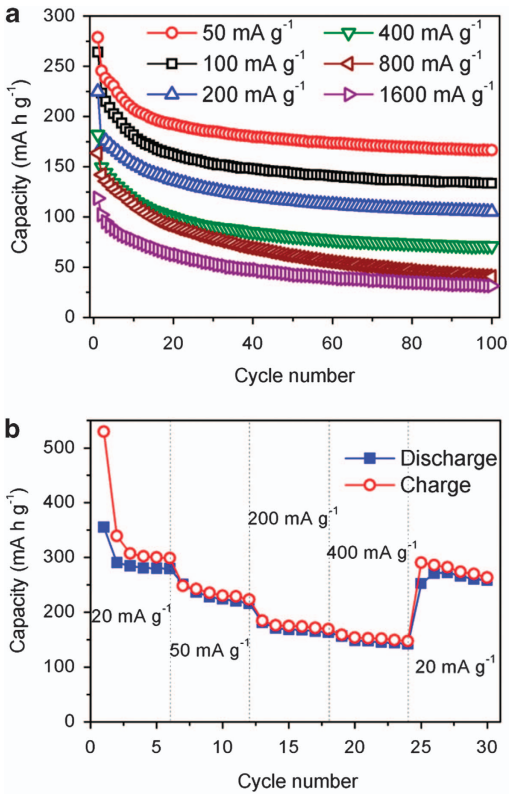

Figure 4 (**a**) Discharge capacity versus cycle number at high current densities of 50, 100, 200, 400, 800 and 1600 mA g^{-1}. (**b**) The rate performance of β-MnO_2 nanorods at varied current densities.

current density was increased to 1600 mA g^{-1}. The β-MnO_2 nanorod electrodes maintained stable cycling performances over 100 cycles at high current densities (166 mAh g^{-1} at 50 mA g^{-1}, 135 mAh g^{-1} at 100 mA g^{-1}, 105 mAh g^{-1} at 200 mA g^{-1} and 71 mAh g^{-1} at 400 mA g^{-1}, respectively). This high-rate performance is superior than that of previously reported β-MnO_2, used as cathode Li-ion storage in Li-ion batteries.[24–26] Furthermore, the cycling performances of β-MnO_2 nanorod electrodes were also tested under varied current densities: 20, 50, 200 and 400 mA g^{-1} (Figure 4b). It should be noted that as long as the current density reversed back to the low current density, the cell capacity recovered to the original values, indicating that the integrity of β-MnO_2 nanorods had been preserved, even after the high-rate cycling.

DISCUSSION

The good electrochemical performance of β-MnO_2 nanorods as cathodes in the Na-ion batteries can be ascribed to its unique crystal structure with high-density (1 × 1) tunnels presented on the exposed (111) facets. β-MnO_2 consists of a 1D channel (1 × 1) tunnel structure and has 2 × (1 × 1) tunnels per formula unit with a tunnel density of 0.104 $Å^{-2}$. The (1 × 1) tunnel has a size of 2.3 Å × 2.3 Å, which can not only provide facile transport for Na-ion insertion and extraction but also accommodate Na-ions. Figure 5 shows the illustration of the tunnel structure of the as-prepared β-MnO_2 nanorods. It can be observed that when the as-prepared β-MnO_2 nanorod was turned 42.7° along its [$\bar{1}$10] axis, the (001) crystal plane of β-MnO_2, with the visible 1D (1 × 1) tunnels, is presented (Figures 5a→b). These open tunnels can facilitate Na-ion insertion and extraction (as illustrated in Figures 5c and d and Supplementary Figure S5). Furthermore, the (1 × 1) tunnels can also accommodate the inserted Na-ions. Therefore, the (1 × 1) tunnel structure can effectively prevent structural collapse and local volumetric variation during the charge/discharge process, which enhances the structural stability and cycling performance.[27,28] Consequently, the as-prepared β-MnO_2 nanorods with exposed (1 × 1) tunnel structures can achieve a high-rate performance and durable cyclability as cathodes in Na-ion batteries.

As shown in Figures 3 and 4, the capacities of the β-MnO_2 nanorod electrodes gradually decrease during long-term cycling. It should also be noted that the discharge profiles become sloped upon cycling, which suggests the slow deterioration of the crystallinity of β-MnO_2 nanorods. To explore the mechanism of Na-ion insertion and extraction in β-MnO_2 nanorods, we conducted *ex situ* XRD and TEM measurements. Figure 6 shows the *ex situ* XRD patterns of the β-MnO_2 nanorod electrodes in the fully discharged state (Na-ion insertion) and fully charged state (Na-ion extraction) in the 1st cycle and the 100th cycle. For comparison, the simulated XRD patterns of β-MnO_2, 1 Na inserted β-MnO_2 and $NaMn_2O_4$ are also presented in Figure 6. From the simulated XRD patterns, we can see that the (200), (220) and (002) reflections become more intense, and that the intensity of the (110) reflection decreased with an Na insertion (see the details in Supplementary Figure S6). When analyzing the *ex situ* XRD patterns (Figure 6), it can be observed that the intensities of all (110), (200) and (220) peaks slightly decreased at the 1st and 100th discharged states.

There are differences between the theoretical calculation and the experimental measurements. The reason could be that the theoretical

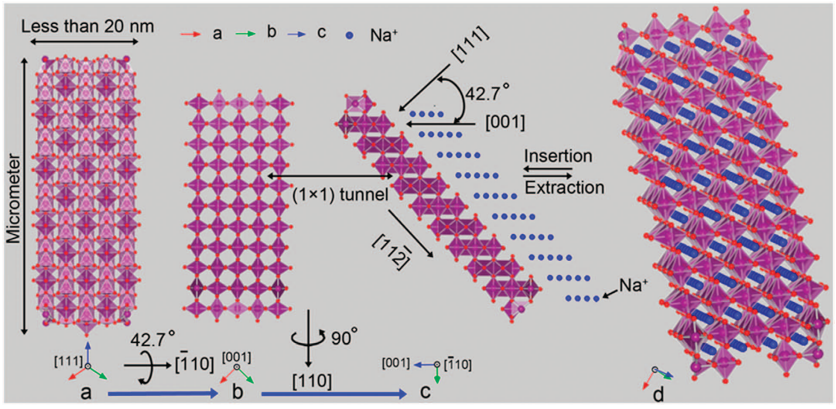

Figure 5 Illustrations of the crystal structure of the as-prepared β-MnO_2 nanorods along the [111] (**a**), [001] (**b**) and [$\bar{1}$10] (**c**) projected directions. (**c**) is a schematic of the Na-ion insertion and extraction in the (1 × 1) tunnels, from which we can see the orientational relationship between the [111] and [001] with a 42.7° interfacial angle. (**d**) is a schematic of a β-MnO_2 nanorod with inserted Na-ions. The Mn, O and Na are colored in purple, red and blue, respectively.

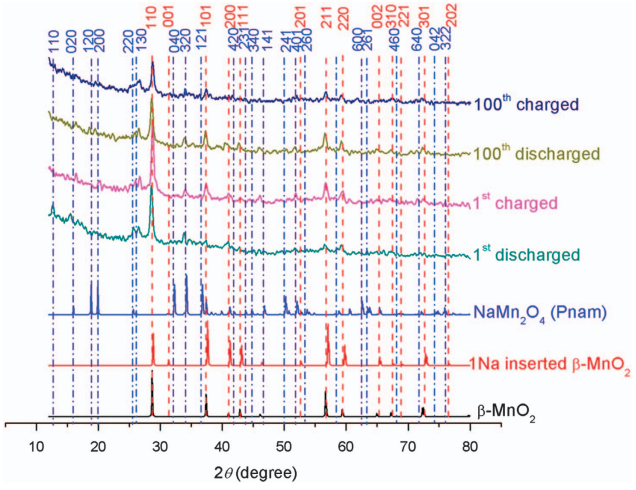

Figure 6 XRD patterns of simulated tetragonal β-MnO_2, 1 Na–inserted β-MnO_2, the orthorhombic $NaMn_2O_4$ phase, and β-MnO_2 nanorod electrodes in the fully discharged state in the 1st cycle (Na-ion insertion), fully charged state in the 1st cycle (Na-ion extraction), fully discharged state in the 100th cycle, and fully charged state in the 100th cycle. The peaks belonging to the β-MnO_2 and 1 Na–inserted β-MnO_2 are marked by red lines, whereas the peaks belonging to the orthorhombic $NaMn_2O_4$ phase are marked by blue lines.

calculation is based on bulk materials, and the preferred orientation of the β-MnO_2 nanorods could affect the change in the relative intensity of diffraction peaks upon Na insertion. We have used the GSAS software suite to calculate the lattice parameters of β-MnO_2 nanorods at the 1st and 100th discharged states (1 Na insertion) based on the diffraction lines of (110), (101) and (111). The results are summarized as follows:

At the 1st discharged state, $a = b = 4.3916$ Å, $c = 2.8740$ Å.
At the 100th discharged state, $a = b = 4.4109$ Å, $c = 2.8756$ Å.

Compared with the lattice parameters of the pristine β-MnO_2 nanorods, $a = b = 4.3880$ Å, $c = 2.8730$ Å, the lattice of β-MnO_2 nanorods slightly expanded after the insertion of 1 Na per formula.

Furthermore, to identify the impurity phase of the by-product generated during the cycling process, we calculated the XRD patterns of all possible $Na_xMn_yO_z$ compounds, including $NaMn_7O_{12}$ (space group: Im3), $Na_2Mn_3O_7$ (space group: P1), $NaMnO_2$ (space group: Pmnmz), $Na_4Mn_2O_5$ (space group: Fdddz), Na_2MnO_4 (space group: P63mc), $Na_{14}Mn_2O_9$ (space group: P3) and $NaMn_2O_4$ (space group: Pnam). The calculated XRD patterns of all the $Na_xMn_yO_z$ compounds and their crystal structures are shown in Supplementary Figures S7a and b , respectively. It was found that the peaks, which do not belong to the β-MnO_2 or Na-inserted β-MnO_2, match the $NaMn_2O_4$ phase (space group: Pnam).

The peaks at 12.8°, 15.8°, 25.5°, 26.1°, 32.3°, 36.8°, 50.25° and 52° correspond to the (110), (020), (220), (130), (040), (121), (241) and (401) crystal planes of $NaMn_2O_4$, respectively. In particular, the high intensity peak at 34.1° in all *ex situ* XRD patterns (Figure 6) should be the (320) plane of $NaMn_2O_4$, which is one of its primary reflection peaks. Moreover, some other peaks overlap with the diffraction peaks of β-MnO_2 or Na-inserted β-MnO_2 (as marked by the blue lines in Figure 6). Therefore, the $NaMn_2O_4$ phase was generated during the discharge and charge process. Although, a small amount of impurity phase $NaMn_2O_4$ was formed, β-MnO_2 nanorods maintained the tetragonal phase during the extended cycling process. This indicates that the β-MnO_2 nanorods are tolerant of the repeated Na ion insertion and extraction.

Ex situ TEM and SAED analyses were also performed on the β-MnO_2 nanorods at the fully discharged and charged states in the 1st and 100th cycles (as shown in Figure 7). It can be observed that the nanorod shape and morphology were preserved for all discharge and charge states (Figures 7a0, b0, c0 and d0). At the fully discharged state in the 1st cycle, the SAED pattern taken from an individual β-MnO_2 nanorod can be indexed along the [001] zone axis of one Na-ion–inserted β-MnO_2 (Figure 7a1), in which the (1$\bar{1}$0), (0$\bar{2}$0), (110), ($\bar{2}\bar{2}$0) and (200) crystal planes can be indexed accurately, whereas the other spot patterns can be indexed as the (020), (040) and (241) crystal planes (with 5.54, 2.77 and 1.81 Å d-spacing, respectively) of the orthorhombic $NaMn_2O_4$ phase.

By further analyzing the lattice-resolved HRTEM image (Figure 7a2) and its corresponding Fast-Fourier-Transform spot patterns, we can directly identify the (110) crystal plane (with approximately 3.1 Å d-spacing) of the Na-ion–inserted β-MnO_2 and the (121) crystal plane (with approximately 2.5 Å d-spacing) of the impurity $NaMn_2O_4$ phase, which confirmed that the formation of impurity $NaMn_2O_4$ occurred in the initial discharge process.

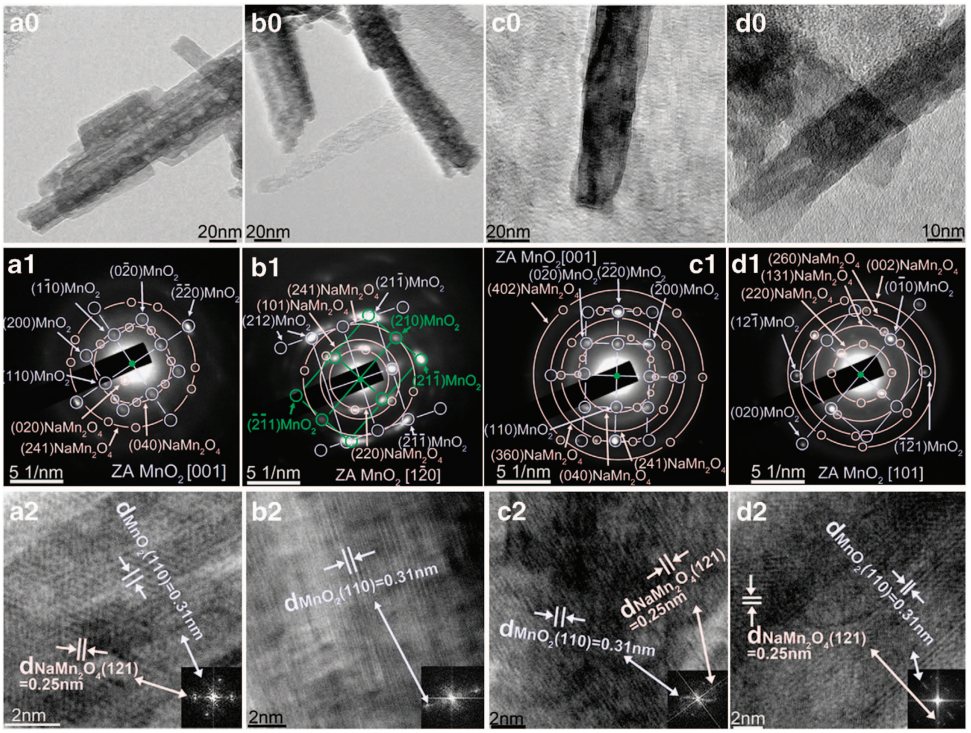

Figure 7 TEM images and SAED patterns of β-MnO_2 nanorods electrodes taken in the fully discharged states (**a0**,**a2**) and fully charged states (**b0–b1**) in the first cycle and the fully discharged (**c0**,**c1**) and fully charged (**d**0,**d**1) states after 100 cycles. **a0**, **b0**, **c0** and **d0** show bright-field TEM images of individual β-MnO_2 nanorods at different stages of the charge and discharge processes. **a1**, **b1**, **c1** and **d1** are the corresponding SAED patterns. **a2**, **b2**, **c2** and **d2** are the lattice-resolved HRTEM images at various stages of the charge and discharge processes. The insets in **a2**, **b2**, **c2** and **d2** are the corresponding fast-Fourier-transform (FFT) patterns.

After being fully charged, the obtained SAED pattern in Figure 7b1 can be indexed as two sets of diffraction patterns along the [1$\bar{2}$0] zone axis of β-MnO_2, where the (210), (21$\bar{1}$) and (212) crystal planes with 1.96, 1.62 and 1.16 Å d-spacing, respectively, can be indexed, indicating the reversible structural recovery of β-MnO_2 after the extraction of Na-ions. From the HRTEM image in Figure 7b2, we observed the (1$\bar{1}$0) crystal plane of β-MnO_2 with a 0.31 nm lattice spacing. The rest of the spot patterns can be indexed as the crystal planes of the $NaMn_2O_4$ phase, including the (220), (101) and (241) with 3.4, 2.7 and 1.81 Å d-spacings, respectively.

These results reveal the irreversible property of the $NaMn_2O_4$ phase, which is the reason for the capacity deterioration of the β-MnO_2 electrode upon cycling. After 100 cycles, the discharged and charged electrodes still preserved their crystalline features, as revealed by the SAED spot patterns (Figures 7c1 and d1). The ($\bar{2}\bar{2}$0), (0$\bar{2}$0) and (110) diffraction spots of Na-ion–inserted β-MnO_2 can be well indexed along the [001] zone axis (Figure 7c1). The (12$\bar{1}$), 0$\bar{1}$0 and (020) diffraction spots of Na-ion extracted β-MnO_2 in the charged state can be clearly indexed along the [101] zone axis. This proved that the crystalline structure of the β-MnO_2 nanorods was retained upon cycling, which is a benefit for the long-term cycling of β-MnO_2 nanorod electrodes. Nevertheless, the impurity phase $NaMn_2O_4$ has been identified in both the SAED patterns (in Figures 7c1 and d1) and the lattice-resolved HRTEM images (Figures 7c2 and d2). This verified that the inactive $NaMn_2O_4$ phase was generated during the cycling process, which is the main cause of the gradual capacity deterioration of the β-MnO_2 electrodes.

In summary, β-MnO_2 nanorods with exposed tunnel structures have been synthesized by a hydrothermal method. TEM, SAED and HRTEM characterization identified that the β-MnO_2 nanorods grow along the [1$\bar{1}$2] direction and have exposed (111) facets. When applied as cathodes in the Na-ion batteries, the β-MnO_2 nanorods delivered a high initial specific capacity of 350 mAh g^{-1} and achieved a good high-rate performance, which could be attributed to the unique crystal structure of β-MnO_2 nanorods with exposed (1 × 1) tunnels that provide facile transport for Na-ion insertion, accommodation and extraction. The mechanisms of Na-ion intercalation and de-intercalation in β-MnO_2 nanorods were studied with *ex situ* XRD and TEM analyses. It was found that the formation of an inactive $NaMn_2O_4$ phase is the main cause of the gradual capacity decrease upon cycling for β-MnO_2 nanorod electrodes.

CONFLICT OF INTEREST

The authors declare no conflict of interest.

ACKNOWLEDGEMENTS

This work was financially supported by the Australian Research Council (ARC) through the ARC FT project (FT110100800). We also acknowledge the support from the National Research Foundation of Korea through the 2013R1A2A1A01015911 project.

1 Palomares, V., Serras, P., Villaluenga, I., Hueso, K. B., Carretero-Gonzalez, J. & Rojo, T. Na-ion batteries, recent advances and present challenges to become low cost energy storage systems. *Energy Environ. Sci.* **5,** 5884–5901 (2012).
2 Ong, S. P., Chevrier, V. L., Hautier, G., Jain, A., Moore, C., Kim, S., Ma, X. H. & Ceder, G. Voltage, stability and diffusion barrier differences between sodium-ion and lithium-ion intercalation materials. *Energy Environ. Sci.* **4,** 3680–3688 (2011).
3 Zaghib, K., Trottier, J., Hovington, P., Brochu, F., Guerfi, A., Mauger, A. & Julien, C. M. Characterization of Na-based phosphate as electrode materials for electrochemical cells. *J. Power Sources* **196,** 9612–9617 (2011).

4 Tepavcevic, S., Xiong, H., Stamenkovic, V. R., Zuo, X., Balasubramanian, M., Prakapenka, V. B., Johnson, C. S. & Rajh, T. Nanostructured bilayered vanadium oxide electrodes for rechargeable sodium-ion batteries. *Acs Nano.* **6,** 530–538 (2012).
5 Cao, Y. L., Xiao, L. F., Wang, W., Choi, D. W., Nie, Z. M., Yu, J. G., Saraf, L. V., Yang, Z. G. & Liu, J. Reversible sodium ion insertion in single crystalline manganese oxide nanowires with long cycle life. *Adv. Mater.* **23,** 3155–3160 (2011).
6 Tevar, A. D., De Graef, M. & Whitacre, J. Cycling-Induced crystallographic and morphological changes in $Na_4Mn_9O_{18}$. *Electrochem. Soc.* **7,** 642–642 (2008).
7 Doeff, M. M., Peng, M. Y., Ma, Y. P. & Jonghe, L. C. D. Orthorhombic Na_xMnO_2 as a cathode material for secondary sodium and lithium polymer batteries. *J. Electrochem. Soc.* **141,** L145–L147 (1994).
8 Gocheva, I. D., Nishijima, M., Doi, T., Okada, S., Yamaki, J. I. & Nishida, T. Mechanochemical synthesis of $NaMF_3$ (M = Fe, Mn, Ni) and their electrochemical properties as positive electrode materials for sodium batteries. *J. Power Sources* **187,** 247–252 (2009).
9 Yamada, Y., Doi, T., Tanaka, I., Okada, S. & Yamaki, J. Liquid-phase synthesis of highly dispersed $NaFeF_3$ particles and their electrochemical properties for sodium-ion batteries. *J. Power Sources* **196,** 4837–4841 (2011).
10 Recham, N., Chotard, J. N., Dupont, L., Djellab, K., Armand, M. & Tarascon, J. M. Ionothermal synthesis of sodium-based fluorophosphate cathode materials. *J. Electrochem. Soc.* **156,** A993–A999 (2009).
11 Tripathi, R., Wood, S., Islam, M. S. & Nazar, L. Na-ion mobility in layered Na_2FePO_4F and olivine Na[Fe, Mn]PO_4. *Energy Environ. Sci.* **6,** 2257–2264 (2013).
12 Ati, M., Dupont, L., Recham, N., Chotard, J. N., Walker, W. T., Davoisne, C., Barpanda, P., Sarou-Kanian, V., Armand, M. & Tarascon, J. M. Synthesis, structural and transport properties of novel bihydrated fluorosulphates $NaMSO_4F$ center dot $2H_2O$ (M = Fe, Co, and Ni). *Chem. Mater.* **22,** 4062–4068 (2010).
13 Barpanda, P., Chotard, J. N., Recham, N., Delacourt, C., Ati, M., Dupont, L., Armand, M. & Tarascon, J. M. Structural, transport, and electrochemical investigation of novel $AMSO_4F$ (A = Na, Li; M = Fe, Co, Ni, Mn) metal fluorosulphates prepared using low temperature synthesis routes. *Inorg. Chem.* **49,** 7401–7413 (2010).
14 Reynaud, M., Barpanda, P., Rousse, G., Chotard, J. N., Melot, B. C., Recham, N. & Tarascon, J. M. Synthesis and crystal chemistry of the $NaMSO_4F$ family (M = Mg, Fe, Co, Cu, Zn). *Solid State Sci.* **14,** 15–20 (2012).
15 Berthelot, R., Carlier, D. & Delmas, C. Electrochemical investigation of the P2-Na_xCoO_2 phase diagram. *Nat. Mater.* **10,** 74–80 (2011).
16 Doeff, M. M., Ma, Y. P., Peng, M. Y., Visco, S. J. & Dejonghe, L. C. in *Energy Environment Economics: 28th Intersociety Energy Conversion Engineering Conference: Papers* Ch. 1 1111–1116 (American Chemical Society, Washington, DC, 1993).
17 Yabuuchi, N., Kajiyama, M., Iwatate, J., Nishikawa, H., Hitomi, S., Okuyama, R., Usui, R., Yamada, Y. & Komaba, S. P2-type $Na_x[Fe_{1/2}Mn_{1/2}]O_2$ made from earth-abundant elements for rechargeable Na batteries. *Nat. Mater.* **11,** 512–517 (2012).
18 Kim, D., Lee, E., Slater, M., Lu, W., Rood, S. & Johnson, C. S. Layered $Na[Ni_{1/3}Fe_{1/3}Mn_{1/3}]O_2$ cathodes for Na-ion battery application. *Electrochem. Commun.* **18,** 66–69 (2012).
19 Komaba, S., Takei, C., Nakayama, T., Ogata, A. & Yabuuchi, N. Electrochemical intercalation activity of layered $NaCrO_2$ vs $LiCrO_2$. *Electrochem. Commun.* **12,** 355–358 (2010).
20 Xia, X. & Dahn, J. R. $NaCrO_2$ is a fundamentally safe positive electrode material for sodium-ion batteries with liquid electrolytes. *Electrochem. Solid-State Lett.* **15,** A1–A4 (2012).
21 Mendiboure, A., Delmas, C. & Hagenmuller, P. Electrochemical intercalation and deintercalation of Na_xMnO_2 bronzes. *J. Solid State Chem.* **57,** 323–331 (1985).
22 Stoyanova, R., Carlier, D., Sendova-Vassileva, M., Yoncheva, M., Zhecheva, E., Nihtianova, D. & Delmas, C. Stabilization of over-stoichiometric Mn^{4+} in layered $Na_{2/3}MnO_2$. *J. Solid State Chem.* **183,** 1372–1379 (2010).
23 Hamani, D., Ati, M., Tarascon, J.-M. & Rozier, P. Na_xVO_2 as possible electrode for Na-ion batteries. *Electrochem. Commun.* **13,** 938–941 (2011).
24 Lee, J., Lee, J. M., Yoon, S., Kim, S. O., Sohn, J. S., Rhee, K. I. & Sohn, H. J. Electrochemical characteristics of manganese oxide/carbon composite as a cathode material for Li/MnO_2 secondary batteries. *J. Power Sources* **183,** 325–329 (2008).
25 Chen, W.-M., Qie, L., Shao, Q. G., Yuan, L. X., Zhang, W. X. & Huang, Y. H. Controllable Synthesis of hollow bipyramid beta-MnO_2 and its high electrochemical performance for lithium storage. *ACS Appl. Mater. Int.* **4,** 3047–3053 (2012).
26 Jiao, F. & Bruce, P. G. Mesoporous crystalline beta-MnO_2: a reversible positive electrode for rechargeable lithium batteries. *Adv. Mater.* **19,** 657–660 (2007).
27 Su, D., Ahn, H.-J. & Wang, G. Hydrothermal synthesis of α-MnO_2 and β-MnO_2 nanorods as high capacity cathode materials for sodium ion batteries. *J. Mater. Chem. A* **1,** 4845–4850 (2013).
28 Devaraj, S. & Munichandraiah, N. Effect of crystallographic structure of MnO_2 on its electrochemical capacitance properties. *J. Phys. Chem. C* **112,** 4406–4417 (2008).

Supplementary Information accompanies the paper on the NPG Asia Materials website (http://www.nature.com/am)